Research Article | Vol. 32, No. 17 / 12 Aug 2024 / Optics Express 29514
Optics EXPRESS

Efficient generation of polarization-entangled photons in metal-organic framework waveguides

Simón Paiva,[1] Rubén A. Fritz,[1] Sanoj Raj,[2,3] Yamil J. Colón,[2] and Felipe Herrera[1,4,*]

[1]Department of Physics, Universidad de Santiago de Chile, Av. Victor Jara 3493, Santiago, Chile
[2]Department of Chemical and Biomolecular Engineering, University of Notre Dame, Notre Dame, IN 46556, USA
[3]Current affiliation: Department of Chemistry, Bowdoin College, Brunswick, ME 04011, USA
[4]Millennium Institute for Research in Optics, Concepción, Chile
*felipe.herrera.u@usach.cl

Abstract: Parametric nonlinear optical processes are instrumental in optical quantum technology for generating entangled light. However, the range of materials conventionally used for producing entangled photons is limited. Metal-organic frameworks (MOFs) have emerged as a novel class of optical materials with customizable nonlinear properties and proven chemical and optical stability. The large number of combinations of metal atoms and organic ligand from which bulk MOF crystals are known to form, facilitates the search of promising candidates for nonlinear optics. To accelerate the discovery of next-generation quantum light sources, we employ a multi-scale modeling approach to study phase-matching conditions for collinear degenerate type-II spontaneous parametric down conversion (SPDC) with MOF-based one dimensional waveguides. Using periodic-density-functional theory calculations to compute the nonlinear optical properties of selected zinc-based MOF crystals, we predict polarization-entangled pair generation rates of order $10^4 - 10^7$ $s^{-1}mW^{-1}$ at 1064 nm for 10 mm crystals, improving the brightness of industry materials such as PPKTP and BBO in some cases. This work underscores the great potential of MOF single crystals as entangled light sources for applications in quantum communication and sensing.

1. Introduction

The genuine quantum correlations in the electromagnetic field that are harnessed in optical quantum technology [1] for secure quantum communication [2–4], quantum sensing [5,6] and quantum information processing [7,8], are ultimately generated through the interaction of classical light with matter. The experimental performance of some quantum optical protocols can often be related to properties of the optical materials used in implementations. For instance, for communication protocols where photon entanglement is critical such as device-independent quantum key distribution [9,10], the secure bit rate can be related to the number of entangled photon pairs generated by a laser-driven nonlinear optical crystal [11–13].

Organic crystals have been studied extensively as candidate nonlinear optical materials due to their intrinsically high nonlinear optical response enabled by electron conjugation [14]. However, due to the relatively weak non-covalent nature of the interactions that drive molecular packing in organic crystals [15], the optical stability of organic optical devices is typically lower than inorganic optical materials such as beta-barium borate (BBO) [16] or lithium niobate ($LiNbO_3$) [17]. In recent years, metal-organic framework (MOF) materials [18,19] have emerged as competitive candidates for nonlinear optics due to their hybrid functional structure that combines the structural and optical stability of inorganic salts with the large nonlinearities of organic

#532747 https://doi.org/10.1364/OE.532747
Journal © 2024 Received 18 Jun 2024; revised 17 Jul 2024; accepted 22 Jul 2024; published 31 Jul 2024

Optics EXPRESS

molecules [20–23]. Experimental demonstrations of large second-order [24–26] and third-order optical nonlinearities [27] with polycrystalline MOF samples have stimulated materials science developments [28–31] that have recently enabled the demonstration of three-wave and four-wave mixing processes with well-defined phase matching in millimeter-scale MOF single crystals [32].

These experimental breakthroughs increase the feasibility of using biaxial MOF single crystals for implementing quantum optical nonlinear processes such as spontaneous parametric down-conversion (SPDC). The generation of photon pairs having energy-time entanglement via type-I SPDC was studied theoretically for zinc-based MOF crystals with tetrazolate ligands [33], using a multi-scale modeling methodology that combines solid-state electronic structure calculations with phenomenological quantum optics theory. The influence of the structural and compositional details of tetrazole-based MOF crystals on the nonlinear efficiency at room temperature was then computationally studied [34], improving our understanding of the design features that are critical for discovering high-performing MOF nonlinear optical devices. This methodology was recently used to screen a publicly available database containing 10^5 MOF crystal structures with known synthetic procedures [35] and identify dozens of MOF candidate materials that are suitable for entangled photon generation in collinear degenerate type-I SPDC [36]. Related modeling approaches have also been used for studying optical nonlinearities in two-dimensional materials [37–39].

In this work, we explore the potential of MOF single crystals as polarization-entangled photon sources, by studying the generation rate and correlation times of entangled photon pairs produced in collinear degenerate type-II SPDC in a single-mode waveguide configuration, as is illustrated in Fig. 1. Waveguides are key optical components in integrated photonics [40,41]. By selecting example crystal structures from a class of non-centrosymmetric zinc-based MOFs of experimental interest [30,32], and comparing their predicted brightness with existing photon pair sources based on periodically-poled potassium titanyl phosphate (PPKTP) and beta-barium borate (BBO),

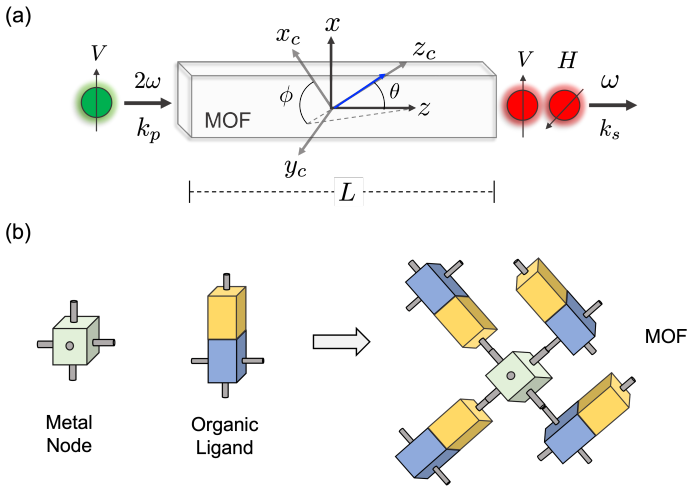

Fig. 1. Entangled photon generation with metal-organic frameworks. (a) Illustration of degenerate collinear type-II SPDC with a single crystal MOF waveguide with length L. Pump photons with wavevector k_p and frequency 2ω enter the waveguide with lab-frame vertical polarization V and produce a pair of polarization entangled photons with vertical and horizonal (H) polarizations in the same input direction, each with frequency ω and wavevector k_s. The crystal optic axis z_c sets a polar angle θ and azimuthal angle ϕ with respect to the propagation direction k. (b) Schematics of the coordination of organic ligands with suitable metal ion nodes to form non-centrosymmetric MOF crystal structures.

Optics EXPRESS

we identify MOF candidates that outperform existing polarization-entangled photon sources in terms of brightness at visible and near-infrared wavelengths, demonstrating the potential of MOF materials as novel quantum light sources in bulk and integrated photonics.

The rest of this work is organized as follows: In Sec. 2, we introduce the MOF crystals studied in this work and review the methodology to evaluate the phase matching conditions in collinear type-II SPDC. In Secs. 3 and 4, we discuss the generation rates of polarization-entangled photon pairs predicted for each MOF crystal and their intrinsic pair correlation times. Comparisons with experimental results for PPKTP waveguides of equivalent dimensions are made. In Sec. 5, we conclude and suggest future research directions.

2. Type-II SPDC with MOF single crystals

Here we describe the phase matching conditions established for type-II SPDC with the MOF crystals studied, report the calculated Sellmeier coefficients for each crystal and describe the effective nonlinearity angular maps at selected signal wavelengths.

2.1. Collinear type-II phase matching for biaxial MOFs

Spontaneous parametric down-conversion (SPDC) [42–44] is a nonlinear optical process in which a pump photon of frequency ω_p and wavevector $\mathbf{k}_p$ is spontaneously converted into a pair of photons with frequencies and wavevectors $(\omega_1, \mathbf{k}_1)$ and $(\omega_2, \mathbf{k}_2)$, upon propagation through an optical medium with non-vanishing second-order optical susceptibility $\chi^{(2)}$ [45]. Energy conservation requires that $\omega_1 + \omega_2 = \omega_p$ and momentum conservation implies the phase matching condition $\mathbf{k}_p = \mathbf{k}_1 + \mathbf{k}_2$. The waves involved in the mixing process have a specific polarization configuration that determines the type of phase matching implemented.

Under conditions of type-II phase matching, the polarization state of one of the output photons is parallel to that of the pump and the second photon in the output pair has orthogonal polarization [46,47]. Denoting the plane that contains the pump ray $\mathbf{k}_p$ and crystal optic axis (OA) as the extraordinary direction (e) and the axis orthogonal to it as the ordinary direction (o), in a type-II SPDC process the polarization combinations (oeo, ooe, eoe, eeo) are allowed for the waves at (ω_p, ω_1 ω_2), respectively. The relative strength of these wave-mixing channels is given by the combined influence of the orientation of the pump rate and polarization relative to the incidence face of the crystal and the contraction of the nonlinear susceptibility tensor with the input and output polarization states. The latter determines the effective nonlinear coefficient [46]

$$d_{\text{eff}} \equiv \chi^{(2)}_{ijk} E_i(\omega_p) E_j(\omega_1) E_k(\omega_2), \tag{1}$$

where $E_i(\omega)$ denotes the electric field component of the wave at frequency ω in the cartesian crystal frame ($i = x_c, y_c, z_c$). We follow standard notation and set the optic axis as the z_c direction (see Fig. 1(a)). Given the polar angle θ of optic axis relative to the pump ray and the azimuthal angle ϕ, the vectorial phase matching equation $\Delta\mathbf{k} \equiv \mathbf{k}_p - \mathbf{k}_1 - \mathbf{k}_2 = 0$ implies a biaxial condition for collinear degenerate SPDC given by $(n_{\omega,+} + n_{\omega,-}) = 2n_{2\omega,-}$ [48], where the $n_{\omega,\pm}$ are the propagation indices of the signal and idler photons and $n_{2\omega,-}$ is the pump index. The effective index n_ω for a given propagation direction $\mathbf{k} = (k_x, k_y, k_z)$ is obtained by solving for $x = 1/n_\omega^2$ in [48–50]

$$\frac{k_x^2}{x - n_{x,\omega}^{-2}} + \frac{k_y^2}{x - n_{y,\omega}^{-2}} + \frac{k_z^2}{x - n_{z,\omega}^{-2}} = 0 \tag{2}$$

where $k_x = \sin\theta\cos\phi$, $k_y = \sin\theta\sin\phi$ and $k_z = \cos\phi$. $n_{x,\omega}$, $n_{y,\omega}$ and $n_{z,\omega}$ are the real refractive indices along orthogonal crystal directions, obtained from measurements or electronic structure calculations, as in this work.

We follow standard notation and denote biaxial crystals as negative or positive, depending whether $n_z - n_y > n_y - n_x$ (positive) or $n_y - n_x > n_z - n_y$ (negative) [36,48]. When computing the

Optics EXPRESS

effective nonlinearity of MOF crystals, d_{eff}, the assumed polarization configuration is ooe for positive biaxial, and eoe for negative biaxial.

2.2. MOF Sellmeier coefficients and effective nonlinearities

We follow the procedure in Ref. [33] to compute the refractive indices n_z, n_y and n_x using periodic density-functional theory (DFT) at different wavelengths, for seven non-centrosymmetric MOF crystals: MIRO-101, MIRO-102, MIRO-103, AQOROP, MOFTIL, ECIWAO and OFUWIV. The MOFs in the MIRO group have received experimental interest due the possibility of controlling the growth mechanism using simple additives [28–31]. The other MOF crystals were recently identified as suitable candidates for optical frequency conversion in a large-scale computational screening study [36]. Particularly, OFUWIV crystals have a good trade-off between d_{eff} and bandgap. The chemical composition and crystal properties of all the structures studied here are given in Supplement 1 (SM).

Table 1 shows the corresponding Sellmeier coefficients of the obtained by fitting $\epsilon_{ii}(\lambda)$ to the two-term expression [51]

$$n^2(\lambda) = A + \frac{B_1\lambda^2}{\lambda^2 - C_1} + \frac{B_2\lambda^2}{\lambda^2 - C_2}, \tag{3}$$

where λ is in units of nm. As a representative example, Fig. 2(a) shows the predicted Sellmeier curves for MOF Zn(4-pyridylacrylate)$_2$ (ECIWAO). Figure 2(b) shows the orientations of the pump wave with respect to the crystal optic axis (tuning curves) that give perfect collinear degenerate ooe phase matching for type-II SPDC at 1064 nm and 1546 nm signal wavelengths in ECIWAO. Figure 2(b) serves to design MOF crystal growth protocols. The Sellmeier curves and phase-matching tuning curves for the other MOF crystals are given in the SM.

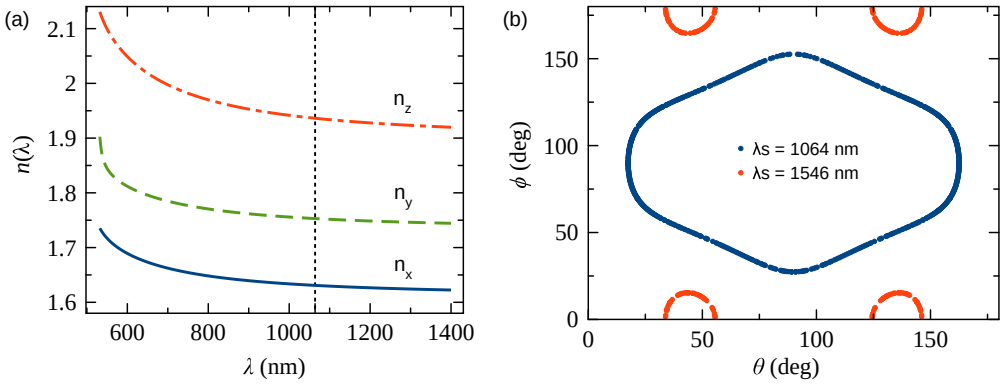

Fig. 2. Sellmeier curves and phase matching conditions for ECIWAO. (a) Theoretical Sellmeier curves for biaxial MOF Zn(4-pyridylacrylate)$_2$ (ECIWAO). (b) Polar and azimuthal angles θ and ϕ with respect to the crystal optic axis z_c that give perfect collinear degenerate phase matching for ECIWAO at 1064 nm (blue circles) and 1546 nm (red circles) signal wavelengths.

As discussed in Sec. 3, the effective nonlinearity d_{eff} of an optical crystal determines the brightness of the down-converted entangled photon source. We compute d_{eff} for each MOF by contracting the calculated second-order susceptibility tensor elements $\chi^{(2)}_{ijk}$ with the unit polarization vectors of the pump and signal waves involved in the type-II SPDC process, according to Eq. (1). The second order tensor susceptibility elements are taken from Refs. [33,36]. Taking again ECIWAO as a representative example, Fig. 3 shows the angular distribution of d_{eff} values (in units of pm/V) along the phase-matching tuning curves in Fig. 2(b). We show nonlinearity mappings for perfect phase matching at 1064 nm signal wavelength in Fig. 3(a) and 1546 nm

Optics EXPRESS

Table 1. Sellmeier coefficients for the refractive index function along orthogonal crystal directions for the seven MOF crystals studied in this work, obtained by fitting periodic DFT calculations to Eq. (3). MIRO-101 and MIRO-103 are uniaxial with $n_x = n_y$. We denote $a \times 10^b \equiv a[b]$.

Crystal	Axis	Type	A	B_1	C_1	B_2	C_2
	n_z		1.7833	8.9000[-3]	1.44323712[5]	3.6470[-1]	4.96202890[4]
MIRO-101	n_x	negative	2.1078	2.5100[-2]	1.41489044[5]	1.0871	5.62150205[4]
	n_z		2.1072	1.4606	1 4.804[4]	9.5309[-2]	1.1700[5]
MIRO-102	n_y	negative	2.1385	1.1527	4.7765[4]	7.6600[-2]	1.1666[5]
	n_x		1.7890	5.030[-2]	1.0701[5]	7.432[-1]	3.584[4]
	n_z		2.0731	1.2882	5.76235328[4]	1.0700[-2]	1.59071640[5]
MIRO-103	n_x	positive	1.9010	5.1430[-1]	5.12308938[4]	4.0800[-2]	1.57385759[5]
	n_z		2.8003	4.2754[-3]	2.588765[5]	1.6691	1.196108[5]
AQOROP	n_y	negative	2.5488	1.1271[-2]	2.615202[5]	9.2632[-1]	9.59809[4]
	n_x		2.0158	0.2528	8.56394[4]	1.91085[-3]	2.643108[5]
	n_z		2.2009	0.2387	1.10517[5]	1.2356	6.3153[4]
MOFTIL	n_y	negative	2.2272	0.20521	1.14011[5]	1.08380	5.9434[4]
	n_x		1.7729	0.5111	3.6259[4]	8.00487[-3]	1.16680[5]
	n_z		1.56880	0.1525	4.5188[4]	1.1823	1.9770 [4]
ECIWAO	n_y	positive	2.2368	0.75972	8.981561[4]	7.18826[-3]	2.7285289[5]
	n_x		1.91004	5.6766[-1]	8.756205[4]	1.31190[-2]	2.446305[5]
	n_z		1.569	0.1525	4.5188 [4]	1.1823	1.9770
OFUWIV	n_y	positive	1.6505	3.3636 [-2]	5.4654 [4]	0.8141	2.3403 [4]
	n_x		1.4569	8.6240 [-2]	4.9653 [4]	0.8962	1.6785 [4]

in Fig. 3(b). These two wavelengths were selected among other possible choices due to their common use in SPDC experiments [45,52]. Optimal nonlinearities $d_{\text{eff}} \approx -8.8$ pm/V at 1064 nm are possible for ECIWAO for signal propagation at $\theta \approx 78°$ and $\phi \approx \{31°, 150°\}$. Nonlinearity maps for other MOF crystals are given in the SM. In general, the magnitude of the nonlinearities predicted for MOFs are comparable with commercial-grade crystals such as KDP (0.38 pm/V), BBO (1.94 pm/V), $LiNbO_3$ (d_{22}=2.47 pm/V) [53], and KTP (3.5 pm/V) [54,55].

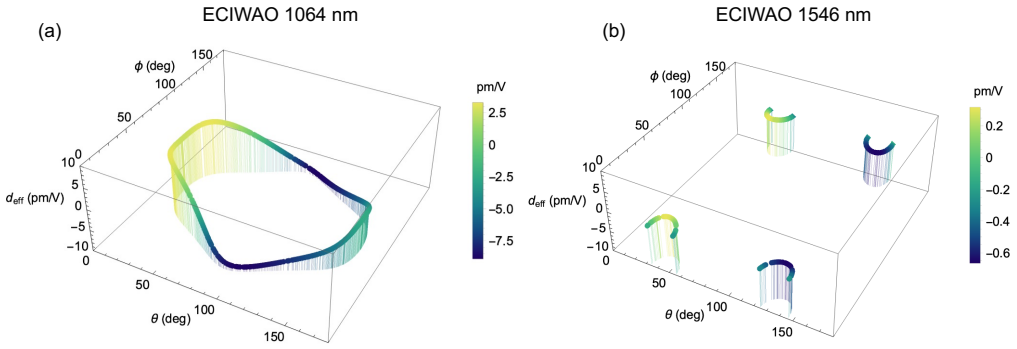

Fig. 3. Effective nonlinearity map. (a) Effective nonlinearity map d_{eff} (in pm/V) for polar and azimuthal angles (θ, ϕ) (in degrees) that give perfect collinear degenerate phase matching for type-II SPDC with ECIWAO crystals at 1064 nm signal wavelength; (b) d_{eff} angular map for 1546 nm signal wavelength.

Optics EXPRESS

3. Polarization-entangled photon pairs

Having established the frequency dependence of the phase mismatch $\Delta\mathbf{k}$ and obtained the effective nonlinearity d_{eff} of a target MOF crystal using *ab-initio* electronic structure calculations, we now use these material parameters to construct a quantum optical description of SPDC that enables an analysis of the temporal correlations of the generated photon pair [33,36] as well as the overall brightness of the entangled photon source in terms of the number of pairs produced per unit time, normalized by pump power.

3.1. Glauber two-time intensity correlation

The spectral and temporal properties of entangled photon pairs produced via SPDC are described by a two-photon wavefunction that for a monochromatic pump and one-dimensional propagation can be written as [43]

$$|\Psi\rangle = A \int d\omega_s \Phi(\Omega_p, \omega_s) \hat{a}_s^\dagger(\Omega_s) \hat{a}_i^\dagger(\omega_p - \omega_s) |0\rangle , \tag{4}$$

where $\hat{a}_s^\dagger$ and $\hat{a}_i^\dagger$ are the field creation operators for the *signal* and *idler* photons in the pair, respectively. Ω_p is the fixed pump frequency and ω_s is the frequency of one of the photons in the pair (e.g., signal). The other photon frequency (idler) is fixed by energy conservation as $\omega_i = \Omega_p - \omega_s$. As discussed below, the constant A encodes the dependence of the two-photon state with physical parameters such as d_{eff}, L, and pump power. For the one-dimensional case discussed here, A also includes the transverse field overlap of the three waves involved [45]. Realistic analysis of the field profiles of pump and signal waves would require solving Maxwell's equations for specific waveguide fabrication geometries [56]. Generalizations of Eq. (4) for other types of phase matching conditions involving three-dimensional field propagation can be found in Refs. [57–62].

The joint spectral amplitude Φ in Eq. (4) is determined by the details of phase mismatch configuration along the propagation direction. For type-II phase matching we have $\Phi(\omega) = \text{sinc}(\omega DL/2) \exp[iDL/2]$, where

$$D = \left.\frac{dk_o}{d\omega_o}\right|_{\Omega_o} - \left.\frac{dk_e}{d\omega_e}\right|_{\Omega_e} \tag{5}$$

is the inverse group velocity difference at the central output frequencies Ω_o and Ω_e, corresponding to the ordinary and the extraordinary waves. For degenerate phase matching we have $\Omega_o = \Omega_e = \Omega_p/2$. k_o and k_e are the ordinary and extraordinary wavenumbers at these frequencies. The wavenumber derivatives can be obtained numerically using the Sellmeier parameters in Table 1.

The probability of two photons to arrive at equally distant photodetectors with delay time τ is given by the two-time Glauber intensity correlation function $G^{(2)}(\tau) = |\langle 0|\hat{E}_1(\tau)\hat{E}_2(0)|\Psi\rangle|^2$ [43,45,57], where $\hat{E}_i(t)$ represents the effective field operator at the detector location. Up to a normalizing constant, the two-photon state in Eq. (4) gives

$$G^{(2)}(\tau) = \left| \int d\nu \, \text{sinc}(\nu DL/2) e^{-\left(\frac{\nu^2}{\sigma^2}\right)} e^{-i\nu\tau} e^{\left(-\frac{i\nu DL}{2}\right)} \right|^2 \tag{6}$$

where the integral is evaluated numerically for a range of detunings ν around $\Omega_p/2$, for an integration bandwidth proportional a few times the characteristic frequency $\nu_L = (DL/2)^{-1}$. σ is the detector bandwidth.

Figure 4 shows the $G^{(2)}$ functions predicted for ECIWAO, AQOROP, MOFTIL and OFUWIV. The assumed detector bandwidth is $\sigma = 1$ nm and crystal length $L = 10$ mm . From the simulated $G^{(2)}$ function, we estimate the length-dependent photon correlation timescale τ_L as the full-width

Optics EXPRESS

half-maximum (FHWM) of the best Gaussian fit, giving values in the range $\tau_L \sim 1-6$ ps for the MOF studied, depending mostly on the amount of birefringence and slopes of the Sellmeier curves at perfect phase matching. The temporal width of $G^{(2)}$ is directly related to the inverse group velocity difference D, which is an intrinsic crystal property [33,43]. Biphoton wavepackets can be engineered by material dispersion to match the timescales of ultrafast electronics [63]. The photon autocorrelation times of the MOFs studied are similar to those of conventional optical crystals [43] for equivalent propagation lengths.

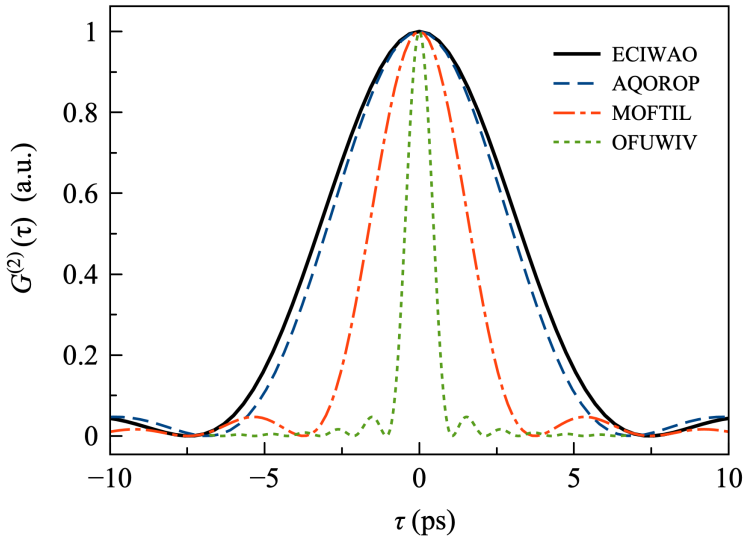

Fig. 4. Intensity autocorrelation functions. $G^{(2)}$ function, normalized to its maximum value, for ECIWAO, AQOROP, MOFTIL and OFUWIV crystals ($L = 10$ mm), under conditions of perfect collinear degenerate type-II phase matching for SPDC at 1064 nm.

3.2. Photon pair generation rates

In order to calculate the absolute pair generation rate via SPDC, the two-photon wavefunction $|\Psi\rangle$ in Eq. (4) needs to be fully characterized in terms of physical parameters. Explicit expressions for the constant prefactor A can be obtained from microscopic derivations based in perturbation theory, assuming three-dimensional wave propagation in the crystal [43,45,57–62].

We follow closely the derivation in Ref. [45] and assume propagation of a monochromatic collimated Gaussian pump beam of wavelength λ_p on a rectangular MOF waveguide with a sub-wavelength transverse area $L_x \times L_y$ and propagation length $L_z \equiv L$ in the millimeter regime (i.e., $L \gg 2\lambda_p$). The waveguide is assumed to support a single guided mode and the transverse intensity profiles of the pump and down-converted light is taken as zeroth-order Hermite-Gaussian modes with characteristic widths w_p (pump), w_s (signal), and w_i (idler). For simplicity, we set signal and idler transverse widths equal ($w_s = w_i$). The counting rate for collinear type-II SPDC is thus [45]

$$R = \frac{|E_p^0|^2 (d_{\text{eff}})^2 L^2}{2\pi c^2} \frac{n_{gs} n_{gi}}{n_s n_i} \left| \frac{w_p^2}{w_s^2 + 2w_p^2} \right|^2 \int d\omega\, \omega\, (\Omega_p - \omega)\, \text{sinc}^2(\Delta k(\omega) L/2) \tag{7}$$

where $|E_p^0| = |D_p^0|/e_o n^2$ is proportional to the monochromatic pump peak magnitude $|D_p^0|$. The power delivered by a Gaussian pump beam is given by $P = c|D_p^0|^2 \pi \sigma_p^2 / n^3 \epsilon_0$. n_s and n_i are the refractive indices of signal and idler fields, respectively. n_{gs} and n_{gi} are the corresponding group

Optics EXPRESS

indices. The frequency-dependent phase mismatch $\Delta k(\omega)$ is obtained from the Sellmeier curves as discussed above, and d_{eff} is evaluated at the optimal polar and azimuthal angles (see Fig. 4(a)) for each MOF. In general, we expect Eq. (7) to underestimate the source brightness by a small geometry-dependent factor, but otherwise giving an accurate order-of-magnitude prediction [45].

Table 2 lists the photon pair generation rates R predicted for selected MOF crystals. For comparison with experiments using rectangular single-mode PPKTP waveguides [45], we set $w_s = 1.875\ \mu$m and $w_p = 0.875\ \mu$m. The band gap E_G and optimal polar and azimuthal angles, and optimal d_{eff} are also reported. The bottom rows show the measured values of R for different implementations of type-II SPDC using PPKTP [45,65,66] and BBO [67] sources of comparable crystal length and generation wavelength.

Table 2. Number of entangled photon pairs (R) generated via SPDC at signal wavelength λ_s per unit second, per milliwatt of pump power, per millimeter crystal length, for the single-mode MOF waveguides studied in this work. The intrinsic two-photon correlation time τ_L, crystal band gap E_G, optic axis polar angle θ and optimal azimuthal angle ϕ for collinear biaxial phase matching are also given. Where MIRO-101 and MIRO-102 are uniaxial crystals, for more information see SM. Selected experimental pair generation rates obtained with PPKTP and BBO crystals are shown for comparison in the bottom rows.

Crystal	λ_s (nm)	L (mm)	R ($\text{s}^{-1}\text{mW}^{-1}$)	$\lvert d_{\text{eff}}\rvert$ (pmV^{-1})	τ_L (ps)	E_G (eV)	θ (deg)	ϕ (deg)
MIRO-101	1064	10	7.4×10^5	0.86	2.5	3.15	28.9	125.22
MIRO-102	1064	10	5.4×10^4	0.29	2.7	3.10	87.88	160.64
MIRO-103	1064	10	3.0×10^4	0.13	2.1	2.98	36.5	29.9
MOFTIL	1064	10	6.2×10^5	1.01	3.2	3.26	116.4	161.9
	1546	10	7.7×10^4	0.38	1.4	3.26	70.22	10.62
AQOROP	1064	10	1.6×10^7	7.38	5.8	2.36	114.76	18.97
	1546	10	1.4×10^5	0.55	1.7	2.36	55.11	55.10
ECIWAO	1064	10	3.1×10^7	8.85	6.3	2.28	102.92	148.66
	1546	10	3.4×10^5	0.67	1.5	2.28	137.95	164.78
OFUWIV	1064	10	2.6×10^6	0.83	0.8	5.07	139.45	168.74
PPKTP [45]	1546	21.2	3.5×10^7	3.18	-	3.52 [64]	-	-
PPKTP [65]	810	30	5.5×10^6	3.18	-	3.52	-	-
PPTKP [66]	800	30	2.36×10^5	3.18	-	3.52	-	-
BBO [67]	762	9	$\approx 7 \times 10^4$	1.5 [68]	-	6.43 [69]	-	-

4. Discussion

The results in the previous section demonstrate the possibility of finding candidate MOF crystals that are as efficient or better than industry-leading PPKTP and BBO in terms of d_{eff} (in pm/V) and absolute pair brightness (in $\text{s}^{-1}\text{mW}^{-1}$). However, these are not necessarily the best metrics when comparing nonlinear optical materials. For example, BBO is nominally less efficient than ECIWAO when values of d_{eff} for type-II SPDC are compared, but its bandgap ($\sim$ 6.4 eV) is much higher than ECIWAO. On average, the bandgap of mono-ligand MOF crystals, like those in Table 2, are about 0.9 eV lower than the HOMO-LUMO gap of the corresponding organic ligand [36]. High bandgaps minimize two-photon absorption heating when pump laser fields are used at visible wavelengths, which in turn allows the use higher pump intensities (larger damage thresholds), leading to higher coincidence counts. From this point of view, OFUWIV offers a favorable combination of relatively high bandgap ($\sim$ 5.1 eV) and large effective nonlinearity (0.9 pm/V).

AQOROP and ECIWAO crystals have values of d_{eff} at 1064 nm exceeding PPKTP twofold or more, but their relatively low band gaps ($\sim$ 2.2 – 2.4 eV) suggests that such high-nonlinear

Optics EXPRESS

performance could be better exploited using longer pump wavelengths (λ_p>800 nm). Since d_{eff} is expected to decrease with increasing wavelength due to dispersion [47] (see also 1546 nm results in Tab. 2), a trade-off between nonlinear efficiency and and bandgap must be found for each material when laboratory implementations are considered. For example, monolayer transition-metal dichalcogenides have very large nonlinearities ($\chi^{(2)} \sim 10^2 - 10^3$ [38]), which compensates the lack of path length for wave-mixing, but have relatively low bandgaps (E_G<0.9 − 2.0 eV).

Tetrazole-based MOF crystals such as MIRO-101, for which growth protocols reaching the millimeter regime are known [30], have sub-optimal conversion efficiencies relative to PPKTP, but compare well with other commonly used optical crystals such as BBO [67] and KDP [70]. Non-porous single crystal MOFs like the ones studied here represent an improvement over conventional organic optical materials in terms of thermochemical stability [71] and heat transport properties [72]. However, to fully assess the potential of this novel optical material class for applications in classical and quantum optics, further studies of the MOF self-assembly process [73] and the optical stability limits of these materials are needed.

High-quality entangled photon sources are enabling tools in photonic quantum technology [1,8]. Modern applications in quantum communication strongly rely on SPDC sources for high-dimensional photonic entanglement and heralded single photons [74], making the prospects for applicability of efficient nonlinear optical materials such as MOFs in next-generation quantum devices highly promising. Recent breakthroughs in MOF crystal engineering have enabled the fabrication of bulk-size crystals that are suitable for free-space quantum optics [30,32], but other quantum applications such as photon triplet generation via third-order SPDC [75–78] are also promising research directions because they do not require millimeter-scale single crystals and could be implemented using polycrystalline samples.

5. Conclusions

We explored non-centrosymmetric MOF single crystals as suitable quantum light source materials. We theoretically studied the features that characterize the indistinguishability and brightness of type-II SPDC entangled photon waveguided sources and identified specific MOF structures with known synthetic procedures that have the potential to exceed the theoretical down-conversion efficiency limits of widely used nonlinear optical crystals such as BBO and PPKTP [79–82]. The predicted polarization-entangled photon pair generation rate of Zn(4-pyridylacrylate)$_2$ waveguides [ECIWAO, Table 2] is higher than some experimental implementations of SPDC with bulk PPKTP crystals of comparable propagation lengths [65,66], which is promising for the stimulating the development of novel MOF-based photonics.

Funding. Agencia Nacional de Investigación y Desarrollo (Fondecyt Postdoctoral 3110857, Fondecyt Regular 1221420, Millennium Science Initiative Program ICN17_012).

Acknowledgments. We thank Esteban Sepúlveda, Gustavo Lima, Stephen Walborn and Dinesh Singh for discussions. S.P., R.A.F. and F.H. thank support from ANID. S.R. and Y.J.C. acknowledge computational resources from the Center for Research Computing (CRC) at Notre Dame.

Disclosures. FH: MAQI Company (I).

Data availability. Data underlying the results presented in this paper are not publicly available at this time but may be obtained from the authors upon reasonable request.

Supplemental document. See Supplement 1 for supporting content.

References

1. J. L. O'Brien, A. Furusawa, and J. Vučković, "Photonic quantum technologies," Nat. Photonics **3**(12), 687–695 (2009).
2. H. J. Kimble, "The quantum internet," Nature **453**(7198), 1023–1030 (2008).
3. S. Wehner, D. Elkouss, and R. Hanson, "Quantum internet: A vision for the road ahead," Science **362**(6412), 1 (2018).

Optics EXPRESS

4. E. Gómez, S. Gómez, I. Machuca, *et al.*, "Multidimensional entanglement generation with multicore optical fibers," Phys. Rev. Appl. **15**(3), 034024 (2021).
5. S. Pirandola, B. R. Bardhan, T. Gehring, *et al.*, "Advances in photonic quantum sensing," Nat. Photonics **12**(12), 724–733 (2018).
6. S. P. Walborn, A. H. Pimentel, L. Davidovich, *et al.*, "Quantum-enhanced sensing from hyperentanglement," Phys. Rev. A **97**(1), 010301 (2018).
7. D. S. Tasca, R. M. Gomes, and F. Toscano, "Continuous-variable quantum computation with spatial degrees of freedom of photons," Phys. Rev. A **83**(5), 052325 (2011).
8. J. Wang, F. Sciarrino, A. Laing, *et al.*, "Integrated photonic quantum technologies," Nat. Photonics **14**(5), 273–284 (2020).
9. I. W. Primaatmaja, K. T. Goh, E. Y.-Z. Tan, *et al.*, "Security of device-independent quantum key distribution protocols: a review," Quantum **7**, 932932 (2023).
10. V. Zapatero, T. van Leent, R. Arnon-Friedman, *et al.*, "Advances in device-independent quantum key distribution," npj Quantum Inf **9**(1), 10 (2023).
11. F. Xu, B. Qi, Z. Liao, *et al.*, "Long distance measurement-device-independent quantum key distribution with entangled photon sources," Appl. Phys. Lett. **103**(6), 061101 (2013).
12. L. Masanes, S. Pironio, and A. Acín, "Secure device-independent quantum key distribution with causally independent measurement devices," Nat. Commun. **2**(1), 238 (2011).
13. W.-Z. Liu, Y.-Z. Zhang, and Y.-Z. Zhen, "Toward a photonic demonstration of device-independent quantum key distribution," Phys. Rev. Lett. **129**(5), 050502 (2022).
14. D. F. Eaton, "Nonlinear Optical Materials," Science **253**(5017), 281–287 (1991).
15. T. e. a. Li, "Crystallization force - a density functional theory concept for revealing intermolecular interactions and molecular packing in organic crystals," Chem. - Eur. J. **15**(2), 361–371 (2009).
16. D. N. Nikogosyan, "Beta barium borate (bbo)," Appl. Phys. A **52**(6), 359–368 (1991).
17. U. Schlarb and K. Betzler, "Refractive indices of lithium niobate as a function of temperature, wavelength, and composition: A generalized fit," Phys. Rev. B **48**(21), 15613–15620 (1993).
18. H. Furukawa, K. E. Cordova, M. O'Keeffe, *et al.*, "The chemistry and applications of metal-organic frameworks," Science **341**(6149), 6149 (2013).
19. Y. J. Colón and R. Q. Snurr, "High-throughput computational screening of metal–organic frameworks," Chem. Soc. Rev. **43**(16), 5735–5749 (2014).
20. C. Wang, T. Zhang, and W. Lin, "Rational synthesis of noncentrosymmetric metal-organic frameworks for second-order nonlinear optics," Chem. Rev. **112**(2), 1084–1104 (2012).
21. L. R. Mingabudinova, V. V. Vinogradov, and V. A. Milichko, "Metal–organic frameworks as competitive materials for non-linear optics," Chem. Soc. Rev. **45**(19), 5408–5431 (2016).
22. R. Medishetty, "Nonlinear optical properties, upconversion and lasing in metal-organic frameworks," Chem. Soc. Rev. **46**(16), 4976–5004 (2017).
23. X. Yang, X. Lin, Y. S. Zhao, *et al.*, "Recent Advances in Micro-Nanostructured Metal–Organic Frameworks towards Photonic and Electronic Applications" (2018).
24. S. Van Cleuvenbergen, I. Stassen, E. Gobechiya, *et al.*, "Zif-8 as nonlinear optical material: Influence of structure and synthesis," Chem. Mater. **28**(9), 3203–3209 (2016).
25. Y.-X. Zhang, B.-X. Li, and H. Lin, "Impressive second harmonic generation response in a novel phase-matchable nlo-active mof derived from achiral precursors," J. Mater. Chem. C **7**(21), 6217–6221 (2019).
26. Z. Chen, G. Gallo, and V. A. Sawant, "Giant enhancement of second harmonic generation accompanied by the structural transformation of 7-fold to 8-fold interpenetrated metal-organic frameworks (mofs)," Angew. Chem., Int. Ed. **59**(2), 833–838 (2020).
27. M. Liu, H. S. Quah, and S. Wen, "Efficient Third Harmonic Generation in a Metal-Organic Framework," Chem. Mater. **28**(10), 3385–3390 (2016).
28. I. Chi-Durán, J. Enríquez, and C. Manquian, "ph-controlled assembly of 3d and 2d zinc-based metal-organic frameworks with tetrazole ligands," ACS Omega **3**(1), 801–807 (2018).
29. J. Enríquez, C. Manquian, and I. Chi-Duran, "Controlled growth of the noncentrosymmetric zn(3-ptz)2 and zn(oh)(3-ptz) metal–organic frameworks," ACS Omega **4**(4), 7411–7419 (2019).
30. J. M. Garcia Garfido, J. Enriquez, I. Chi-Duran, *et al.*, "Millimeter-sized metal-organic framework single crystals without inversion symmetry: Controlled growth and self-assembly mechanism" (2020).
31. I. Chi-Durán, R. A. Fritz, and R. Urzúa-Leiva, "Anisotropic band-edge absorption of millimeter-sized zn(3-ptz)2 single-crystal metal–organic frameworks," ACS Omega **7**(28), 24432–24437 (2022).
32. D. Hidalgo-Rojas, J. García-Garfido, and J. Enríquez, "Phase-coherent optical frequency up-conversion with millimeter-size zn(3-ptz)2 metal-organic framework single crystals," Adv. Opt. Mater. **11**(15), 2300142 (2023).
33. R. A. Fritz, Y. J. Colón, and F. Herrera, "Engineering entangled photon pairs with metal–organic frameworks," Chem. Sci. **12**(10), 3475–3482 (2021).
34. S. Raj, R. A. Fritz, F. Herrera, *et al.*, "Understanding the correlation between structure and entangled photon pair properties with metal–organic frameworks," J. Phys. Chem. C **127**(23), 10987–10996 (2023).
35. C. R. Groom, I. J. Bruno, M. P. Lightfoot, *et al.*, "The Cambridge Structural Database," Acta Crystallogr., Sect. B: Struct. Sci., Cryst. Eng. Mater. **72**(2), 171–179 (2016).

Optics EXPRESS

36. S. Raj, S. Paiva, and R. A. Fritz, "First-principles screening of metal–organic frameworks for entangled photon pair generation," Mater. Quantum. Technol. **4**(1), 015404 (2024).
37. A. Autere, H. Jussila, and A. Marini, "Optical harmonic generation in monolayer group-vi transition metal dichalcogenides," Phys. Rev. B **98**(11), 115426 (2018).
38. N. A. Pike and R. Pachter, "Second-order nonlinear optical properties of monolayer transition-metal dichalcogenides by computational analysis," J. Phys. Chem. C **125**(20), 11075–11084 (2021).
39. P. Su, H. Ye, and N. Sun, "Second harmonic generation in janus transition metal chalcogenide oxide monolayers: A first-principles investigation," Nanomaterials **13**(14), 2150 (2023).
40. Y. Tang, Q. Luo, Y. Chen, *et al.*, "All-silicon photoelectric biosensor on chip based on silicon nitride waveguide with low loss," Nanomaterials **13**(5), 914 (2023).
41. A. G. Leal-Junior and C. Marques, "Diaphragm-embedded optical fiber sensors: A review and tutorial," IEEE Sens. J. **21**(11), 12719–12733 (2021).
42. Y. H. Shih and C. O. Alley, "New type of einstein-podolsky-rosen-bohm experiment using pairs of light quanta produced by optical parametric down conversion," Phys. Rev. Lett. **61**(26), 2921–2924 (1988).
43. Y. Shih, "Entangled biphoton source - property and preparation," Rep. Prog. Phys. **66**(6), 1009–1044 (2003).
44. T. E. Kiess, Y. H. Shih, A. V. Sergienko, *et al.*, "Einstein-podolsky-rosen-bohm experiment using pairs of light quanta produced by type-ii parametric down-conversion," Phys. Rev. Lett. **71**(24), 3893–3897 (1993).
45. J. Schneeloch, S. H. Knarr, and D. F. Bogorin, "Introduction to the absolute brightness and number statistics in spontaneous parametric down-conversion," J. Opt. **21**(4), 043501 (2019).
46. R. W. Boyd, *Nonlinear Optics* (Elsevier, 2008), 3rd ed.
47. W. Zhang, H. Yu, H. Wu, *et al.*, "Phase-matching in nonlinear optical compounds: A materials perspective," Chem. Mater. **29**(7), 2655–2668 (2017).
48. J. Yao and T. S. Fahlen, "Calculations of optimum phase match parameters for the biaxial crystal ktiopo4," J. Appl. Phys. **55**(1), 65–68 (1984).
49. H. Ito, H. Naito, and H. Inaba, "Generalized study on angular dependence of induced second-order nonlinear optical polarizations and phase matching in biaxial crystals," J. Appl. Phys. **46**(9), 3992–3998 (1975).
50. G. Huo, Y. Wang, and M. Zhang, "An effective method for calculating phase-matching conditions in biaxial crystals," Appl. Phys. B **120**(2), 239–246 (2015).
51. G. Ghosh, "Sellmeier coefficients and dispersion of thermo-optic coefficients for some optical glasses," Appl. Opt. **36**(7), 1540–1546 (1997).
52. T. Landes, M. Allgaier, and S. Merkouche, "Experimental feasibility of molecular two-photon absorption with isolated time-frequency-entangled photon pairs," Phys. Rev. Res. **3**(3), 033154 (2021).
53. V. G. Dmitriev, G. G. Gurzadyan, and D. N. Nikogosyan, *Handbook of Nonlinear Optical Crystals* (Springer, 2013), vol. 64, pp. 122,125.
54. R. C. Eckardt and R. L. Byer, "Measurement of nonlinear optical coefficients by phase-matched harmonic generation," in *Inorganic Crystals for Optics, Electro-Optics, and Frequency Conversion*, vol. 1561 P. F. Bordui, ed., International Society for Optics and Photonics (SPIE, 1991), pp. 119–127.
55. I. Shoji, T. Kondo, and A. Kitamoto, "Absolute scale of second-order nonlinear-optical coefficients," J. Opt. Soc. Am. B **14**(9), 2268–2294 (1997).
56. S. M. Spillane, M. Fiorentino, and R. G. Beausoleil, "Spontaneous parametric down conversion in a nanophotonic waveguide," Opt. Express **15**(14), 8770–8780 (2007).
57. G. Boucher, T. Douce, and D. Bresteau, "Toolbox for continuous-variable entanglement production and measurement using spontaneous parametric down-conversion," Phys. Rev. A **92**(2), 023804 (2015).
58. M. Fiorentino, S. M. Spillane, and R. G. Beausoleil, "Spontaneous parametric down-conversion in periodically poled ktp waveguides and bulk crystals," Opt. Express **15**(12), 7479–7488 (2007).
59. L. Hutter, E. S. Gómez, G. Lima, *et al.*, "Partially coherent spontaneous parametric downconversion: Twisted Gaussian biphotons," AVS Quantum Science **3**(3), 031401 (2021).
60. S. P. Walborn and A. H. Pimentel, "Generalized hermite–gauss decomposition of the two-photon state produced by spontaneous parametric down conversion," J. Phys. B: At., Mol. Opt. Phys. **45**(16), 165502 (2012).
61. S. P. Walborn, A. N. de Oliveira, R. S. Thebaldi, *et al.*, "Entanglement and conservation of orbital angular momentum in spontaneous parametric down-conversion," Phys. Rev. A **69**(2), 023811 (2004).
62. A. V. Burlakov, M. V. Chekhova, O. A. Karabutova, *et al.*, "Collinear two-photon state with spectral properties of type-i and polarization properties of type-ii spontaneous parametric down-conversion: Preparation and testing," Phys. Rev. A **64**(4), 041803 (2001).
63. A. Valencia, M. V. Chekhova, A. Trifonov, *et al.*, "Entangled two-photon wave packet in a dispersive medium," Phys. Rev. Lett. **88**(18), 183601 (2002).
64. F. Yang, L. Huang, and X. Zhao, "An energy band engineering design to enlarge the band gap of ktiopo4 (ktp)-type sulfates via aliovalent substitution," J. Mater. Chem. C **7**(26), 8131–8138 (2019).
65. E. Brambila, R. Gómez, and R. Fazili, "Ultrabright polarization-entangled photon pair source for frequency-multiplexed quantum communication in free-space," Opt. Express **31**(10), 16107–16117 (2023).
66. Omshankar, V. Venkataraman, and J. Ghosh, "Bright source of narrowband polarization-entangled photons from a thick type-ii ppktp crystal," Opt. Express **32**(3), 3470–3479 (2024).

Optics EXPRESS

67. P. Trojek and H. Weinfurter, "Collinear source of polarization-entangled photon pairs at nondegenerate wavelengths," Appl. Phys. Lett. **92**(21), 211103 (2008).
68. R. Klein, G. Kugel, and A. Maillard, "Absolute non-linear optical coefficients measurements of bbo single crystal and determination of angular acceptance by second harmonic generation," Opt. Mater. **22**(2), 163–169 (2003).
69. R. H. French, J. W. Ling, F. S. Ohuchi, *et al.*, "Electronic structure of $\beta - bab_2o_4$ and lib_3o_5 nonlinear optical crystals," Phys. Rev. B **44**(16), 8496–8502 (1991).
70. P. J. Mosley, J. S. Lundeen, and B. J. Smith, "Heralded generation of ultrafast single photons in pure quantum states," Phys. Rev. Lett. **100**(13), 133601 (2008).
71. S. Neogi, *Metal-Organic Frameworks: Single-Crystal-to-Single-Crystal Transformations* (John Wiley and Sons, 2014), pp. 1–50.
72. H. Babaei, A. J. H. McGaughey, and C. E. Wilmer, "Effect of pore size and shape on the thermal conductivity of metal-organic frameworks," Chem. Sci. **8**(1), 583–589 (2017).
73. Y. J. Colón, A. Z. Guo, and L. W. Antony, "Free energy of metal-organic framework self-assembly," The Journal of Chemical Physics **150**(10), 104502 (2019).
74. J. C. ne, G. C. nas, and P. Skrzypczyk, "Multi-core fiber integrated multi-port beam splitters for quantum information processing," Optica **7**(5), 542–550 (2020).
75. M. Corona, K. Garay-Palmett, and A. B. U'Ren, "Experimental proposal for the generation of entangled photon triplets by third-order spontaneous parametric downconversion in optical fibers," Opt. Lett. **36**(2), 190–192 (2011).
76. M. Corona, K. Garay-Palmett, and A. B. U'Ren, "Third-order spontaneous parametric down-conversion in thin optical fibers as a photon-triplet source," Phys. Rev. A **84**(3), 033823 (2011).
77. M. G. Moebius, F. Herrera, and S. Griesse-Nascimento, "Efficient photon triplet generation in integrated nanophotonic waveguides," Opt. Express **24**(9), 9932–9954 (2016).
78. A. Cavanna, J. Hammer, and C. Okoth, "Progress toward third-order parametric down-conversion in optical fibers," Phys. Rev. A **101**(3), 033840 (2020).
79. T. Zhong, F. N. C. Wong, A. Restelli, *et al.*, "Efficient single-spatial-mode ppktp waveguide source for high dimensional entanglement-based qkd," in *Conference on Lasers and Electro-Optics* (2012), pp. 1–2.
80. M. Jachura, M. Karpiński, C. Radzewicz, *et al.*, "High-visibility nonclassical interference of photon pairs generated in a multimode nonlinear waveguide," Opt. Express **22**(7), 8624–8632 (2014).
81. D. Cozzolino, B. Da Lio, D. Bacco, *et al.*, "High-dimensional quantum communication: Benefits, progress, and future challenges," Adv. Quantum Technol. **2**(12), 1900038 (2019).
82. S. Gómez, E. S. Gómez, and O. Jiménez, "Experimental quantum state discrimination using the optimal fixed rate of inconclusive outcomes strategy," Sci. Rep. **12**(1), 17312 (2022).